



Originally published as:

Esmaili, M., Motagh, M., Hooper, A. (2017): Application of Dual-Polarimetry SAR Images in Multitemporal InSAR Processing. - *IEEE Geoscience and Remote Sensing Letters*, 14, 9, pp. 1489—1493.

DOI: <http://doi.org/10.1109/LGRS.2017.2717846>

# Application of Dual-Polarimetry SAR Images in Multitemporal InSAR Processing

Mostafa Esmaili, Mahdi Motagh, and Andy Hooper

**Abstract**—Multitemporal polarimetric synthetic aperture radar (SAR) data can be used to estimate the dominant scattering mechanism of targets in a stack of SAR data and to improve the performance of SAR interferometric methods for deformation studies. In this letter, we developed a polarimetric form of amplitude difference dispersion (ADD) criterion for time-series analysis of pixels in which interferometric noise shows negligible decorrelation in time and space in small baseline algorithm. The polarimetric form of ADD is then optimized in order to find the optimum scattering mechanism of the pixels, which in turn is used to produce new interferograms with better quality than single-pol SAR interferograms. The selected candidates are then combined with temporal coherency criterion for final phase stability analysis in full-resolution interferograms. Our experimental results derived from a data set of 17 dual polarizations X-band SAR images (HH/VV) acquired by TerraSAR-X shows that using optimum scattering mechanism in the small baseline method improves the number of pixel candidates for deformation analysis by about 2.5 times in comparison with the results obtained from single-channel SAR data. The number of final pixels increases by about 1.5 times in comparison with HH and VV in small baseline analysis. Comparison between persistent scatterer (PS) and small baseline methods shows that with regards to the number of pixels with optimum scattering mechanism, the small baseline algorithm detects 10% more pixels than PS in agricultural regions. In urban regions, however, the PS method identifies nearly 8% more coherent pixels than small baseline approach.

**Index Terms**—Amplitude difference dispersion (ADD), polarimetric optimization, slowly decorrelating filtered phase (SDFP), Tehran plain.

## I. INTRODUCTION

INTERFEROMETRIC analysis of synthetic aperture radar (SAR) data is a powerful geodetic technique to measure surface deformations [1]–[4]. The accuracy achieved with interferometric measurements depends on a variety of factors including temporal and geometrical decorrelation, variations in atmospheric water vapor between SAR data acquisitions and the accuracy of orbital and digital elevation model used in the processing [5]. In order to address these limitations, multitemporal InSAR (MTI) time-series processing techniques such as small baseline algorithms and persistent scatterer InSAR<sub>s</sub> (PSI) have been developed.

Manuscript received March 11, 2017; revised June 5, 2017; accepted June 13, 2017. (Corresponding author: Mostafa Esmaili.)

M. Esmaili is with the School of Surveying and Geospatial Engineering, College of Engineering, University of Tehran, Tehran, Iran (e-mail: maesmaili@ut.ac.ir).

M. Motagh is with the GFZ German Research Center for Geosciences, Department of Geodesy, Remote Sensing Section, 14473 Potsdam, and also with the Institute for Photogrammetry and GeoInformation, Leibniz Universität Hannover, 30167 Hannover, Germany (e-mail: Motagh@gfz.potsdam.de).

A. Hooper is with COMET, School of Earth and Environment, University of Leeds, Leeds LS2 9JT, U.K. (e-mail: a.hooper@leeds.ac.uk).

Color versions of one or more of the figures in this letter are available online at <http://ieeexplore.ieee.org>.

Digital Object Identifier 10.1109/LGRS.2017.2717846

The main goal of these techniques is to identify pixels for which the effect of the interferometric noise is small, so that they remain stable over the whole period of SAR data acquisition [6]–[8].

The PSI technique, first proposed by Ferretti *et al.* [6], [7], presents a solution to deal with spatiotemporal decorrelations of interferometric phase using time-series analysis of single-master interferograms. The technique uses amplitude dispersion index (ADI) as a proxy of phase stability to identify pixels whose scattering properties are coherent between SAR image acquisition with long time interval and different look angles, the so-called permanent scatterer (PS). As interferograms are generated with a common master, PSs are limited to those pixels that show high coherence even in interferograms with larger baselines than the critical baseline [6], [7]. In [8], a new PS technique was proposed in which both amplitude and phase criteria are assessed to determine the stability of PSs. An initial set of candidate pixel based on amplitude analysis is selected first and then in an iterative process, the PS probability is refined using phase analysis. The method is more suitable for detecting low-amplitude PS pixels in natural terrains, where the relationship between ADI index and phase stability breaks down.

Small baseline techniques use interferograms with small temporal and spatial baselines to reduce decorrelation. The original small baseline technique [9] uses a network of multilooked small baseline interferograms and the target scatterers are identified by coherence (i.e., complex correlation) criterion [10], [11]. The multilooking is a limiting factor for detecting local deformations. This issue was resolved in [12] with an extended version of small baseline algorithm applied on full-resolution SAR data set. Hooper [13] proposed another new small baseline method in which full-resolution differential interferograms are used to identify stable scatterers incorporating both amplitude and phase criterion. The filtered phase of those pixels that decorrelate little over short time intervals of interferograms, the so-called slowly-decorrelating filtered phase (SDFP) pixels are then used for deformation analysis.

Polarimetric optimization of polarimetric SAR data has been applied to improve classical InSAR results [14], [15] in terms of both deformation estimation and target classification [16], [17]. Optimization can be applied to full polarimetric space-borne SAR data [18], [19], ground-based fully PolSAR acquisitions [20] or compact polarimetric SAR data [21]–[23]. The approach improves the results by finding the scattering mechanism that minimizes decorrelation for each pixel over time, using coherence stability criteria or ADI, thereby maximizing the quality and number of selected PS pixels [17], [22], [24]–[26].

In this letter, for the first time, we have developed a polarimetric optimization approach based on the small baseline

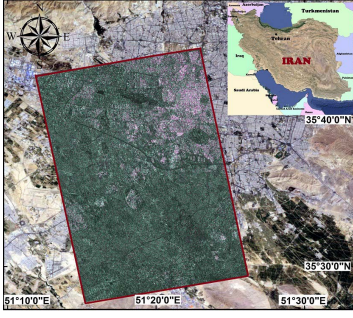


Fig. 1. RGB composite of study area produced by amplitude of dual-pol TerraSAR-SX images over Tehran plain ( $R = HH$  channel,  $G = VV$  channel and  $B = HH - VV$  channel) overlaid on Google-Earth image.

94 method of the Stanford method for persistent scatterers (PSs)  
 95 and multitemporal InSAR (StaMPS/MTI) analysis presented  
 96 in [13]. In our algorithm, instead of applying ADI criterion,  
 97 we utilize simulated annealing (SA) optimization to minimize  
 98 the amplitude difference dispersion (ADD) value of each pixel.  
 99 This can be employed as a rough proxy for phase variance for  
 100 Gaussian scatterer pixels and it is an indicator for potential  
 101 of a pixel to be an SDFP candidate, in dual-polarimetry  
 102 X-band SAR images, followed by projection of the polarimetric  
 103 interferograms onto the optimized polarimetric channel  
 104 to reproduce the interferograms with the optimum scattering  
 105 mechanism. As proposed in [17], SDFP candidates are selected  
 106 based on lower values of ADD in reproduced interferograms.  
 107 In an additional step, the phase stability of each candidate is  
 108 tested using a measure similar to coherence magnitude called  
 109 temporal coherence [8], [13] and SDFP pixels are extracted.  
 110 Time-series analysis and 3-D phase unwrapping are then  
 111 carried out to retrieve the deformation parameters. We evaluate  
 112 the method with a data set consisting of 17 dual polarization  
 113 X-band SAR data (HH/VV) acquired by TerraSAR-X satellite  
 114 between July 2013 and January 2014 over Tehran plain,  
 115 Iran (Fig. 1).

## 116 II. PIXEL SELECTION IN MULTITEMPORAL InSAR

117 In the StaMPS small baseline method, a set of candi-  
 118 date pixels for time-series analysis are first selected based  
 119 on the amplitudes of SAR interferograms, to reduce the  
 120 computational cost time. An index called ADD has been  
 121 presented ( $D_{\Delta A}$ ) to identify SDFP candidates [13]

$$122 D_{\Delta A} = \frac{\sigma_{\Delta a}}{\bar{a}} = \frac{\sqrt{\sum_{i=1}^N (\Delta A_i - \overline{\Delta A})^2 / N}}{\sum_{i=1}^N (|M_i| + |S_i|) / 2N} \quad (1)$$

123 where  $\sigma_{\Delta a}$  is the standard deviation of the difference in ampli-  
 124 tude between master and slave images,  $\bar{a}$  is the mean ampli-  
 125 tude,  $\Delta A_i$  is the difference in amplitude between master ( $M_i$ )  
 126 and slave ( $S_i$ ) images, and  $N$  is the number of interferograms.  
 127 In this method a higher value of ADD in comparison with  
 128 ADI, e.g., 0.6 is selected for the threshold and pixels with  
 129 ADD value less than the threshold are considered as SDFP  
 130 candidates. The residual phase noise for SDFP candidates is  
 131 estimated by subtracting two major components of signal:  
 132 spatially correlated and spatially uncorrelated components.  
 133 Finally, SDFP pixels are identified among the candidates using

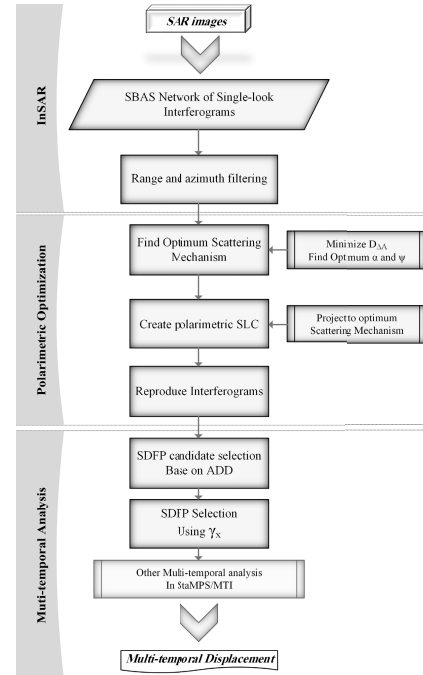


Fig. 2. Flowchart of the overall process in our study.

temporal coherence [8], [13], defined as 134

$$135 \gamma_x = \frac{1}{N} \left| \sum_{i=1}^N \exp \{ j(\varphi_{x,i} - \tilde{\varphi}_{x,i} - \Delta \hat{\varphi}_{\theta,x,i}^u) \} \right| \quad (2)$$

136 where  $\varphi_{x,i}$  is the wrapped phase of pixel  $x$  in the  $i$ th interfer-  
 137 ograms,  $\tilde{\varphi}_{x,i}$  is the estimate for the spatially correlated terms,  
 138  $\Delta \hat{\varphi}_{\theta,x,i}^u$  is the estimate of the spatially uncorrelated look angle  
 139 error term, and  $N$  is the number of interferograms.

140 For dual-pol SAR data we need to extend the ADD in (1),  
 141 which is applicable only for single-pol data, also to include  
 142 dual-pol data and optimize it to increase the density of SDFP  
 143 pixels for the time-series analysis. We then apply temporal  
 144 coherence in (2) to identify the SDFP pixels.

145 Fig. 2 shows a flowchart of the overall processing strategy  
 146 that is implemented in this letter. The method consists of three  
 147 main steps: 1) InSAR processing; 2) polarimetric optimization;  
 148 and (3) multitemporal analysis of the optimized interferograms.  
 149 Single-pol multitemporal InSAR analysis includes only  
 150 InSAR processing (step 1) and time-series analysis of the  
 151 interferograms (step 3). Polarimetric optimization is used here  
 152 to improve the performance of this analysis using dual-pol  
 153 data. In Section III we describe in detail the methodology we  
 154 used in our study.

## 155 III. ADD OPTIMIZATION

156 In order to obtain the polarimetric form of ADD it is  
 157 sufficient to replace the amplitude of single-pol data in (1)  
 158 by the polarimetric scattering coefficient,  $\mu$  defined as

$$159 \mu = \omega^{*T} \underline{K} \quad (3)$$

$$160 \underline{K} = \frac{1}{\sqrt{2}} [S_{hh} + S_{vv}, S_{hh} - S_{vv}]^T \quad (4)$$

$$161 \underline{\omega} = [\cos(\alpha) \quad \sin(\alpha) e^{j\psi}]^T, \quad 0 \leq \alpha \leq \pi/2, \quad -\pi \leq \psi \leq \pi \quad (5)$$

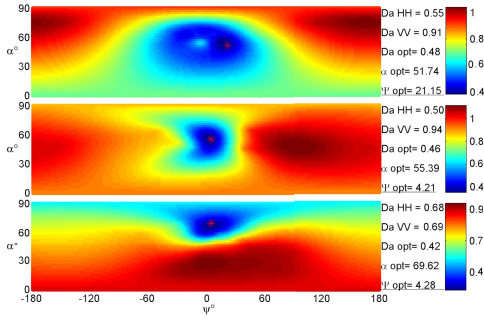


Fig. 3. Values of ADD for all possible values for  $\alpha$  and  $\psi$ , for three arbitrarily selected pixels. The red star presents the minimum value of ADD.

where  $K$  stands for the polarimetric vector,  $\omega$  is the polarimetric projection vector,  $S_{VV}$  and  $S_{HH}$  are the complex values of the HH and VV channels, respectively,  $T$  is the transpose operator and  $*$  denotes the conjugate operator.  $\alpha$  and  $\psi$  are Pauli parameters which represent the scattering mechanism [17], [22], [27]. The polarimetric form of ADD in (1) can then be written in the following form:

$$D_{\Delta A}^{\text{Pol}} = \frac{\sqrt{\sum_{i=1}^N (\Delta A_i^{\text{Pol}} - \overline{\Delta A^{\text{Pol}}})^2 / N}}{\sum_{i=1}^N (|\omega^{*T} K_i^M| + |\omega^{*T} K_i^S|) / 2N}$$

$$\Delta A^{\text{Pol}} = |\omega^{*T} K^M| - |\omega^{*T} K^S| \quad (6)$$

where  $K_i^M$  and  $K_i^S$  are polarimetric vectors of master and slave images, respectively.

The main objective of polarimetric optimization is to find the optimum scattering mechanism of the pixels and generate interferograms with better quality than using single-pol SAR images. To simplify the search of the optimum scattering mechanism, we parameterized the projection vector in terms of Pauli basis parameters. In order to build consistent time series of phases related to deformation we assume that the scattering mechanisms of the pixels remain the same during acquisition time, as in the case of multibaseline equal scattering mechanism. Therefore,  $\omega$  would be the same for the pixel in whole stack of interferograms [28].

The optimization problem is to find the projection vector that minimizes the value of ADD. Fig. 3 illustrates the possible ADD values, in terms of  $\alpha$  and  $\psi$ , for three arbitrarily selected pixels in our study area. In [17] we showed that SA is an effective method to minimize such smooth functions as illustrated in Fig. 3 and to find the optimum  $\alpha$  and  $\psi$  in their corresponding finite range. We define a coarse grid with a step size of  $10^\circ$  for both  $\alpha$  and  $\psi$  and search for the values that give the minimum ADD. These values for  $\alpha$  and  $\psi$  are then used as initial values in the SA optimization method.

#### IV. EXPERIMENTAL RESULTS AND DISCUSSION

To evaluate the method we processed 17 co-polar SAR images acquired by the TerraSAR-X satellite in an ascending mode between July 2013 and January 2014 over the Tehran plain, which is highly affected by subsidence [29]. We formed a small baseline network consisting of 44 single-look interferograms as shown in Fig. 4. We then generated interferograms for HH, VV and optimum channels and calculated the ADD value of each pixel in the single-look interferograms. To evaluate the improvement in ADD, we compared

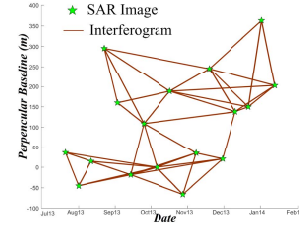


Fig. 4. Small baselines network used in this letter. The stars denote the SAR images and lines present the formed interferograms for Small Baseline processing.

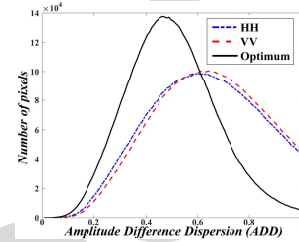


Fig. 5. Histograms of ADD for HH, VV and optimum channel.

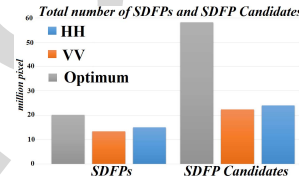


Fig. 6. Number of SDFP Candidates and SDFP pixels, obtained by HH, VV and optimum channel.

the histograms of ADD values for HH, VV and optimum channel (Fig. 5).

As shown in Fig. 5, by applying the proposed method, the histogram of ADD values in optimum channel is inclined to lower values of ADD in comparison to HH and VV channels. Therefore, by thresholding ADD value of less than 0.6, more SDFP candidates are extracted in optimum channel as compared to single-pole interferograms.

Fig. 6 depicts the number of selected SDFP candidates obtained from HH, VV and optimum channels using ADD criterion and also the improvement in number of SDFP pixels after utilizing temporal coherency.

The total number of SDFP candidates for the optimum channel is about 2.5 times higher than for the HH and VV channels. Considering the final selection of SDFP pixels for the optimum channel, the number has increased by about 1.4 times and 1.6 times in comparison to the HH and VV channels, respectively.

In order to evaluate the efficiency of using multitemporal polarimetric SAR data for different models of scattering we made a comparison between urban and nonurban regions. 46% of our study area comprises urban region, while the nonurban portion is about 54%. In urban areas, the number of identified candidates using the optimum channel is increased by  $\sim 1.7$  and  $\sim 2.1$  times compared to HH and VV channels, respectively. In regard to the agricultural regions, the increase is  $\sim 2.1$  and  $\sim 2.2$  times [Fig. 7(b)]. The number of final SDFP pixels increased  $\sim 1.4$  and  $\sim 1.5$  times in urban regions and  $\sim 1.48$  and  $\sim 1.65$  times in agricultural regions, in comparison

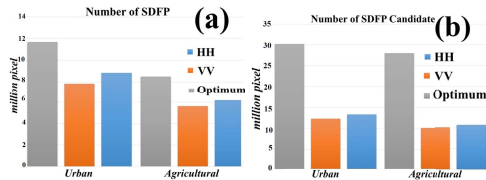


Fig. 7. Number of (a) identified SDFP pixels and (b) SDFP candidates detected in urban and agricultural regions using HH, VV and optimum.

TABLE I

QUANTITATIVE COMPARISON OF IDENTIFIED SDFP PIXELS WITH RESPECT TO PS PIXELS (EXPRESSED IN PERCENT OF PS PIXELS)

Dataset	Agricultural	Urban
HH	8.5 %	-9.0 %
VV	8.2 %	-8.9 %
Optimum	10.3 %	-7.9 %

to HH and VV channels, respectively [Fig. 7(a)]. Therefore the proposed algorithm is slightly more successful in nonurban regions than in urban regions.

As PS pixels and SDFP pixels relate to different scattering characteristics of the ground, we also compared the density of measurements for both of the methods in urban and nonurban regions. Table I describes the percentage of additional pixels identified by SDFP pixels in comparison with PS pixels for which the results were previously published in [17]. For the HH and VV channels we detect about 8% more SDFP pixels than PS in agricultural regions, however, over the urban area the number of identified SDFPs is almost 9% less than PS pixels.

Similar to the HH and VV channels, in the case of the optimum channel, the small baseline method detects 10% more coherent pixels in agricultural regions, while in urban area the PS pixels are more numerous than SDFP pixels by about 8%. SDFP pixels show little loss of correlation in short time intervals whereas PS pixels remain stable over the whole period of data acquisition. Therefore, in nonurban area more SDFP pixels are expected to be identified than PS pixels. By contrast, in urban areas PS pixels are more abundant. This might be related to the effect of filtering in the small baseline method, which increases the decorrelation in pixels dominated by a single scatterer as a result of coarsening the resolution of spectra [13].

In order to check that using the optimum channel leads to lower phase noise, we selected SDFP pixels approximately every  $0.001^\circ$  in both directions, and calculated the variance of the phase differences between the selected pixels and their immediate SDFP neighbors for the optimum, HH and VV channels. The results are shown in Fig. 8.

The standard deviation of differences are very similar for HH and VV, but are generally lower for the optimum channel, indicating that our method leads to reduced phase noise. There appear to be two populations of pixels, however; those for which the improvement is marginal and those for which the improvement is more significant [indicated in Fig 8(a)]. This division is not apparently related to scattering mechanism, but does appear to correlate with spatial position (Fig. 9), with pixels in urban areas, plotted in red, more likely to fall in the population with greatest improvement.

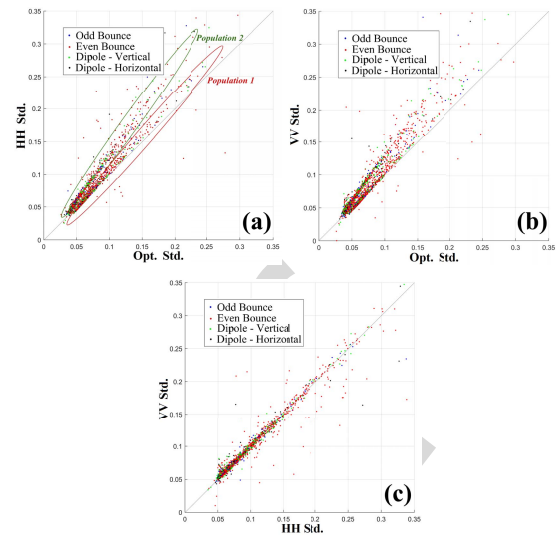


Fig. 8. Cross comparison of Standard deviation of phase differences of nearby SDFP pixels for the selected SDFP pixels for (a) HH versus Optimum channel, the two populations marked by green and red ellipse are spatially located in Fig. 9, (b) VV versus optimum channel, and (c) HH versus VV channel. Blue and red dots indicate odd-bounce and even-bounce scattering mechanisms, respectively. Green and black colors indicate vertical and horizontal dipole scattering mechanism, respectively.

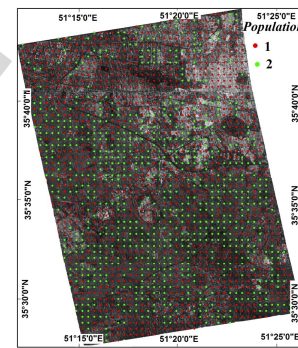


Fig. 9. Spatial position of the pixels in the two populations indicated in Fig. 8(a). Red circles depict the pixels located in the population where the reduction in standard deviation is most significant and the other population members are drawn in green.

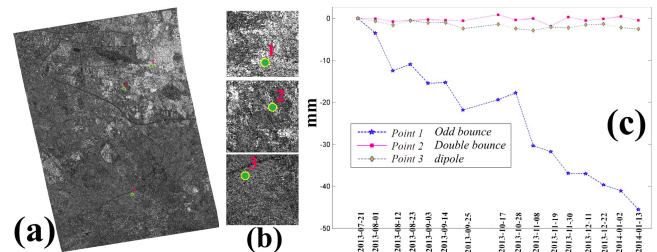


Fig. 10. (a) Location of the three points which detected by our method but not by using HH and VV. (b) Closer look of he points in (a), point 1 is located in a farming zone and shows odd-bounce mechanism, point 2 is located in an urban area with the dominant scattering mechanism for the pixel being double bounce and point 3 is a dipole. (c) Time series plot of the selected points.

Fig. 10 shows the time series for three sample SDFP pixels with odd-bounce (point 1), even-bounce (point 2) and dipole (point 3) scattering mechanisms, respectively,

that were selected using the optimal channel, but not when using HH and VV channels. The smoothness of each of the time series indicates that the phase values have a low contribution from noise and that our algorithm is not increasing the number of selected pixels simply by selecting more noisy pixels.

## V. CONCLUSION

StaMPS is a powerful method for multitemporal analysis of single-channel SAR images [13]. In this letter, we have presented a small baseline method, implemented in StaMPS, to deal with dual polarization SAR images. The ADD index criterion is first minimized for dual polarimetric data to find the optimum scattering mechanism that lead to increase the number of SDFP candidates. Then the results are combined with temporal coherence criteria to select final coherent pixels for time-series analysis. Our experiment in both urban and agricultural regions, shows that applying our method for dual-pol data increased the number of SDFP pixels by 50% in comparison to single-pol data InSAR time-series analysis. In addition, the assessment between the result of our proposed method for small baseline algorithm with those from PS-InSAR polarimetric optimization [17], showed that the density of SDFP pixels, in small baseline approach, is more than PS pixels in nonurban regions, while, in urban area the number of PS pixels is slightly higher than the SDFP pixels. Future research could focus on implementing this type of polarimetric optimization on full/quad polarimetry SAR images. Also, joint optimization using the PSI approach [17], [22] and our new algorithm could improve the ability to find stable points for a large range of ground scattering characteristics.

## ACKNOWLEDGMENT

Copyright of TerraSAR-X data belongs to German Aerospace Agency (DLR) and the data were provided by the project Motagh\_XTI\_LAND505.

## REFERENCES

- [1] F. Amelung, D. L. Galloway, J. W. Bell, H. A. Zebker, and R. J. Lacznik, "Sensing the ups and downs of Las Vegas: InSAR reveals structural control of land subsidence and aquifer-system deformation," *Geology*, vol. 27, no. 6, pp. 483–486, 1999.
- [2] G. Fornaro, A. Pauciuolo, and F. Serafino, "Deformation monitoring over large areas with multipass differential SAR interferometry: A new approach based on the use of spatial differences," *Int. J. Remote Sens.*, vol. 30, no. 6, pp. 1455–1478, 2009.
- [3] D. Massonnet *et al.*, "The displacement field of the Landers earthquake mapped by radar interferometry," *Nature*, vol. 364, no. 6433, pp. 138–142, Jul. 1993.
- [4] M. Motagh *et al.*, "Subduction earthquake deformation associated with 14 November 2007, Mw 7.8 Tocopilla earthquake in Chile: Results from InSAR and aftershocks," *Tectonophysics*, vol. 490, nos. 1–2, pp. 60–68, 2010.
- [5] H. A. Zebker and J. Villasenor, "Decorrelation in interferometric radar echoes," *IEEE Trans. Geosci. Remote Sens.*, vol. 30, no. 5, pp. 950–959, Sep. 1992.
- [6] A. Ferretti, C. Prati, and F. Rocca, "Nonlinear subsidence rate estimation using permanent scatterers in differential SAR interferometry," *IEEE Trans. Geosci. Remote Sens.*, vol. 38, no. 5, pp. 2202–2212, May 2000.
- [7] A. Ferretti, C. Prati, and F. Rocca, "Permanent scatterers in SAR interferometry," *IEEE Trans. Geosci. Remote Sens.*, vol. 39, no. 1, pp. 8–20, Jan. 2001.
- [8] A. Hooper, H. Zebker, P. Segall, and B. Kampes, "A new method for measuring deformation on volcanoes and other natural terrains using InSAR persistent scatterers," *Geophys. Res. Lett.*, vol. 31, no. 23, 2004.
- [9] P. Berardino, G. Fornaro, R. Lanari, and E. Sansosti, "A new algorithm for surface deformation monitoring based on small baseline differential SAR interferograms," *IEEE Trans. Geosci. Remote Sens.*, vol. 40, no. 11, pp. 2375–2383, Nov. 2002.
- [10] O. Mora, J. J. Mallorqui, and A. Broquetas, "Linear and nonlinear terrain deformation maps from a reduced set of interferometric SAR images," *IEEE Trans. Geosci. Remote Sens.*, vol. 41, no. 10, pp. 2243–2253, Oct. 2003.
- [11] D. A. Schmidt and R. Bürgmann, "Time-dependent land uplift and subsidence in the Santa Clara valley, California, from a large interferometric synthetic aperture radar data set," *J. Geophys. Res. Solid Earth*, vol. 108, no. B9, Sep. 2003.
- [12] R. Lanari, O. Mora, M. Manunta, J. J. Mallorqui, P. Berardino, and E. Sansosti, "A small-baseline approach for investigating deformations on full-resolution differential SAR interferograms," *IEEE Trans. Geosci. Remote Sens.*, vol. 42, no. 7, pp. 1377–1386, Jul. 2004.
- [13] A. Hooper, "A multi-temporal InSAR method incorporating both persistent scatterer and small baseline approaches," *Geophys. Res. Lett.*, vol. 35, no. 16, Aug. 2008.
- [14] S. R. Cloude and K. P. Papathanassiou, "Polarimetric SAR interferometry," *IEEE Trans. Geosci. Remote Sens.*, vol. 36, no. 5, pp. 1551–1565, Sep. 1998.
- [15] E. Colin, C. Titin-Schnaider, and W. Tabbara, "An interferometric coherence optimization method in radar polarimetry for high-resolution imagery," *IEEE Trans. Geosci. Remote Sens.*, vol. 44, no. 1, pp. 167–175, Jan. 2006.
- [16] P. Dheenathayalan and R. Hanssen, "Target characterization and interpretation of deformation using persistent scatterer interferometry and polarimetry," in *Proc. 5th Int. Workshop Sci. Appl. SAR Polarimetry Polarimetric Interferometry (PolinSAR)*, 2011, pp. 1–8.
- [17] M. Esmaeili and M. Motagh, "Improved persistent scatterer analysis using amplitude dispersion index optimization of dual polarimetry data," *J. Photogramm. Remote Sens.*, vol. 117, pp. 108–114, Jul. 2016.
- [18] S. Alipour, K. F. Tiampo, S. Samsonov, and P. J. Gonzalez, "Multi-baseline PolInSAR using RADARSAT-2 quad-pol data: Improvements in interferometric phase analysis," *IEEE Geosci. Remote Sens. Lett.*, vol. 10, no. 6, pp. 1280–1284, Nov. 2013.
- [19] D. Monells, J. Mallorqui, G. Centolanza, and C. Lopez-Martinez, "Application of polarimetric techniques in DinSAR processing for space borne subsidence monitoring," in *Proc. Sci. Appl. SAR Polarimetry Polarimetric Interferometry (PolinSAR)*, vol. 695, 2011, pp. 1–22.
- [20] L. Pipia *et al.*, "Polarimetric differential SAR interferometry: First results with ground-based measurements," *IEEE Geosci. Remote Sens. Lett.*, vol. 6, no. 1, pp. 167–171, Jan. 2009.
- [21] V. D. Navarro-Sanchez and J. M. López-Sanchez, "Subsidence monitoring using polarimetric persistent scatterers interferometry," in *Proc. IEEE Int. Geosci. Remote Sens. Symp. (IGARSS)*, Jul. 2011, pp. 1083–1086.
- [22] V. D. Navarro-Sanchez and J. M. Lopez-Sanchez, "Improvement of persistent-scatterer interferometry performance by means of a polarimetric optimization," *IEEE Geosci. Remote Sens. Lett.*, vol. 9, no. 4, pp. 609–613, Jul. 2012.
- [23] V. D. Navarro-Sanchez, J. M. Lopez-Sanchez, and L. Ferro-Famil, "Polarimetric approaches for persistent scatterers interferometry," *IEEE Trans. Geosci. Remote Sens.*, vol. 52, no. 3, pp. 1667–1676, Mar. 2014.
- [24] S. Samsonov and K. Tiampo, "Polarization phase difference analysis for selection of persistent scatterers in SAR interferometry," *IEEE Geosci. Remote Sens. Lett.*, vol. 8, no. 2, pp. 331–335, Mar. 2011.
- [25] R. Iglesias, D. Monells, X. Fabregas, J. J. Mallorqui, A. Aguiasca, and C. López-Martinez, "Phase quality optimization in polarimetric differential SAR interferometry," *IEEE Trans. Geosci. Remote Sens.*, vol. 52, no. 5, pp. 2875–2888, May 2014.
- [26] B. Wu, T. Ling, Y. Chen, and H. Lei, "New methods in multibaseline polarimetric SAR interferometry coherence optimization," *IEEE Geosci. Remote Sens. Lett.*, vol. 12, no. 10, pp. 2016–2020, Oct. 2015.
- [27] S. R. Cloude and K. P. Papathanassiou, "Polarimetric optimisation in radar interferometry," *Electron. Lett.*, vol. 33, no. 13, pp. 1176–1178, Jun. 1997.
- [28] M. Neumann, L. Ferro-Famil, and A. Reigber, "Multibaseline polarimetric SAR interferometry coherence optimization," *IEEE Geosci. Remote Sens. Lett.*, vol. 5, no. 1, pp. 93–97, Jan. 2008.
- [29] M. Motagh *et al.*, "Land subsidence in Iran caused by widespread water reservoir overexploitation," *Geophys. Res. Lett.*, vol. 35, no. 16, Aug. 2008.

## AUTHOR QUERIES

### AUTHOR PLEASE ANSWER ALL QUERIES

**PLEASE NOTE:** We cannot accept new source files as corrections for your paper. If possible, please annotate the PDF proof we have sent you with your corrections and upload it via the Author Gateway. Alternatively, you may send us your corrections in list format. You may also upload revised graphics via the Author Gateway.

Please be aware that authors are required to pay overlength page charges (\$200 per page) if the paper is longer than 3 pages. If you cannot pay any or all of these charges please let us know.

This pdf contains 2 proofs. The first half is the version that will appear on Xplore. The second half is the version that will appear in print. If you have any figures to print in color, they will be in color in both proofs.

The “Open Access” option for your paper expires when the paper is published on Xplore in an issue with page numbers. Papers in “Early Access” may be changed to Open Access.

If you have not completed your electronic copyright form (ECF) and payment option please return to Scholar One “Transfer Center.” In the Transfer Center you will click on “Manuscripts with Decisions” link. You will see your article details and under the “Actions” column click “Transfer Copyright.” From the ECF it will direct you to the payment portal to select your payment options and then return to ECF for copyright submission.

AQ:1 = Please provide the expansion for “InSAR.”

AQ:2 = Please provide the postal code for “University of Tehran, Tehran, Iran.”

AQ:3 = Please provide the country name for “the GFZ German Research Center for Geosciences.”

AQ:4 = Please confirm whether the retention of this sentence in the acknowledgment section is ok.

AQ:5 = Please provide the page range for refs. [8], [11], [13], and [29].

AQ:6 = Please confirm the author names, article title, conference title, volume no., page range, and year for ref. [19].

# Application of Dual-Polarimetry SAR Images in Multitemporal InSAR Processing

Mostafa Esmaili, Mahdi Motagh, and Andy Hooper

**Abstract**—Multitemporal polarimetric synthetic aperture radar (SAR) data can be used to estimate the dominant scattering mechanism of targets in a stack of SAR data and to improve the performance of SAR interferometric methods for deformation studies. In this letter, we developed a polarimetric form of amplitude difference dispersion (ADD) criterion for time-series analysis of pixels in which interferometric noise shows negligible decorrelation in time and space in small baseline algorithm. The polarimetric form of ADD is then optimized in order to find the optimum scattering mechanism of the pixels, which in turn is used to produce new interferograms with better quality than single-pol SAR interferograms. The selected candidates are then combined with temporal coherency criterion for final phase stability analysis in full-resolution interferograms. Our experimental results derived from a data set of 17 dual polarizations X-band SAR images (HH/VV) acquired by TerraSAR-X shows that using optimum scattering mechanism in the small baseline method improves the number of pixel candidates for deformation analysis by about 2.5 times in comparison with the results obtained from single-channel SAR data. The number of final pixels increases by about 1.5 times in comparison with HH and VV in small baseline analysis. Comparison between persistent scatterer (PS) and small baseline methods shows that with regards to the number of pixels with optimum scattering mechanism, the small baseline algorithm detects 10% more pixels than PS in agricultural regions. In urban regions, however, the PS method identifies nearly 8% more coherent pixels than small baseline approach.

**Index Terms**—Amplitude difference dispersion (ADD), polarimetric optimization, slowly decorrelating filtered phase (SDFP), Tehran plain.

## I. INTRODUCTION

INTERFEROMETRIC analysis of synthetic aperture radar (SAR) data is a powerful geodetic technique to measure surface deformations [1]–[4]. The accuracy achieved with interferometric measurements depends on a variety of factors including temporal and geometrical decorrelation, variations in atmospheric water vapor between SAR data acquisitions and the accuracy of orbital and digital elevation model used in the processing [5]. In order to address these limitations, multitemporal InSAR (MTI) time-series processing techniques such as small baseline algorithms and persistent scatterer InSAR (PSI) have been developed.

Manuscript received March 11, 2017; revised June 5, 2017; accepted June 13, 2017. (Corresponding author: Mostafa Esmaili.)

M. Esmaili is with the School of Surveying and Geospatial Engineering, College of Engineering, University of Tehran, Tehran, Iran (e-mail: maesmaili@ut.ac.ir).

M. Motagh is with the GFZ German Research Center for Geosciences, Department of Geodesy, Remote Sensing Section, 14473 Potsdam, and also with the Institute for Photogrammetry and GeoInformation, Leibniz Universität Hannover, 30167 Hannover, Germany (e-mail: Motagh@gfz.potsdam.de).

A. Hooper is with COMET, School of Earth and Environment, University of Leeds, Leeds LS2 9JT, U.K. (e-mail: a.hooper@leeds.ac.uk).

Color versions of one or more of the figures in this letter are available online at <http://ieeexplore.ieee.org>.

Digital Object Identifier 10.1109/LGRS.2017.2717846

The main goal of these techniques is to identify pixels for which the effect of the interferometric noise is small, so that they remain stable over the whole period of SAR data acquisition [6]–[8].

The PSI technique, first proposed by Ferretti *et al.* [6], [7], presents a solution to deal with spatiotemporal decorrelations of interferometric phase using time-series analysis of single-master interferograms. The technique uses amplitude dispersion index (ADI) as a proxy of phase stability to identify pixels whose scattering properties are coherent between SAR image acquisition with long time interval and different look angles, the so-called permanent scatterer (PS). As interferograms are generated with a common master, PSs are limited to those pixels that show high coherence even in interferograms with larger baselines than the critical baseline [6], [7]. In [8], a new PS technique was proposed in which both amplitude and phase criteria are assessed to determine the stability of PSs. An initial set of candidate pixel based on amplitude analysis is selected first and then in an iterative process, the PS probability is refined using phase analysis. The method is more suitable for detecting low-amplitude PS pixels in natural terrains, where the relationship between ADI index and phase stability breaks down.

Small baseline techniques use interferograms with small temporal and spatial baselines to reduce decorrelation. The original small baseline technique [9] uses a network of multilooked small baseline interferograms and the target scatterers are identified by coherence (i.e., complex correlation) criterion [10], [11]. The multilooking is a limiting factor for detecting local deformations. This issue was resolved in [12] with an extended version of small baseline algorithm applied on full-resolution SAR data set. Hooper [13] proposed another new small baseline method in which full-resolution differential interferograms are used to identify stable scatterers incorporating both amplitude and phase criterion. The filtered phase of those pixels that decorrelate little over short time intervals of interferograms, the so-called slowly-decorrelating filtered phase (SDFP) pixels are then used for deformation analysis.

Polarimetric optimization of polarimetric SAR data has been applied to improve classical InSAR results [14], [15] in terms of both deformation estimation and target classification [16], [17]. Optimization can be applied to full polarimetric space-borne SAR data [18], [19], ground-based fully PolSAR acquisitions [20] or compact polarimetric SAR data [21]–[23]. The approach improves the results by finding the scattering mechanism that minimizes decorrelation for each pixel over time, using coherence stability criteria or ADI, thereby maximizing the quality and number of selected PS pixels [17], [22], [24]–[26].

In this letter, for the first time, we have developed a polarimetric optimization approach based on the small baseline



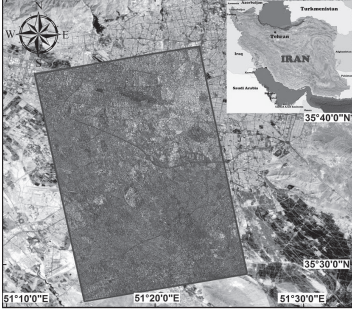


Fig. 1. RGB composite of study area produced by amplitude of dual-pol TerraSAR-SX images over Tehran plain ( $R = HH$  channel,  $G = VV$  channel and  $B = HH - VV$  channel) overlaid on Google-Earth image.

94 method of the Stanford method for persistent scatterers (PSs)  
 95 and multitemporal InSAR (StaMPS/MTI) analysis presented  
 96 in [13]. In our algorithm, instead of applying ADI criterion,  
 97 we utilize simulated annealing (SA) optimization to minimize  
 98 the amplitude difference dispersion (ADD) value of each pixel.  
 99 This can be employed as a rough proxy for phase variance for  
 100 Gaussian scatterer pixels and it is an indicator for potential  
 101 of a pixel to be an SDFP candidate, in dual-polarimetry  
 102 X-band SAR images, followed by projection of the polarimetric  
 103 interferograms onto the optimized polarimetric channel  
 104 to reproduce the interferograms with the optimum scattering  
 105 mechanism. As proposed in [17], SDFP candidates are selected  
 106 based on lower values of ADD in reproduced interferograms.  
 107 In an additional step, the phase stability of each candidate is  
 108 tested using a measure similar to coherence magnitude called  
 109 temporal coherence [8], [13] and SDFP pixels are extracted.  
 110 Time-series analysis and 3-D phase unwrapping are then  
 111 carried out to retrieve the deformation parameters. We evaluate  
 112 the method with a data set consisting of 17 dual polarization  
 113 X-band SAR data (HH/VV) acquired by TerraSAR-X satellite  
 114 between July 2013 and January 2014 over Tehran plain,  
 115 Iran (Fig. 1).

## 116 II. PIXEL SELECTION IN MULTITEMPORAL InSAR

117 In the StaMPS small baseline method, a set of candi-  
 118 date pixels for time-series analysis are first selected based  
 119 on the amplitudes of SAR interferograms, to reduce the  
 120 computational cost time. An index called ADD has been  
 121 presented ( $D_{\Delta A}$ ) to identify SDFP candidates [13]

$$122 D_{\Delta A} = \frac{\sigma_{\Delta a}}{\bar{a}} = \frac{\sqrt{\sum_{i=1}^N (\Delta A_i - \overline{\Delta A})^2 / N}}{\sum_{i=1}^N (|M_i| + |S_i|) / 2N} \quad (1)$$

123 where  $\sigma_{\Delta a}$  is the standard deviation of the difference in ampli-  
 124 tude between master and slave images,  $\bar{a}$  is the mean ampli-  
 125 tude,  $\Delta A_i$  is the difference in amplitude between master ( $M_i$ )  
 126 and slave ( $S_i$ ) images, and  $N$  is the number of interferograms.  
 127 In this method a higher value of ADD in comparison with  
 128 ADI, e.g., 0.6 is selected for the threshold and pixels with  
 129 ADD value less than the threshold are considered as SDFP  
 130 candidates. The residual phase noise for SDFP candidates is  
 131 estimated by subtracting two major components of signal:  
 132 spatially correlated and spatially uncorrelated components.  
 133 Finally, SDFP pixels are identified among the candidates using

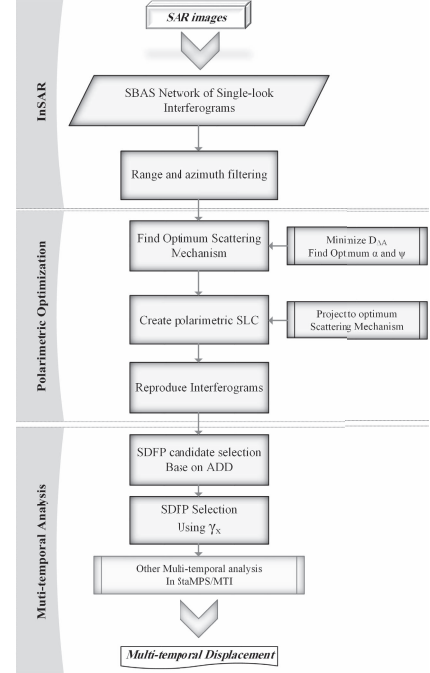


Fig. 2. Flowchart of the overall process in our study.

temporal coherence [8], [13], defined as

$$134 \gamma_x = \frac{1}{N} \left| \sum_{i=1}^N \exp \{ j(\varphi_{x,i} - \tilde{\varphi}_{x,i} - \Delta \hat{\varphi}_{\theta,x,i}^u) \} \right| \quad (2) \quad 135$$

136 where  $\varphi_{x,i}$  is the wrapped phase of pixel  $x$  in the  $i$ th interfer-  
 137 ograms,  $\tilde{\varphi}_{x,i}$  is the estimate for the spatially correlated terms,  
 138  $\Delta \hat{\varphi}_{\theta,x,i}^u$  is the estimate of the spatially uncorrelated look angle  
 139 error term, and  $N$  is the number of interferograms.

140 For dual-pol SAR data we need to extend the ADD in (1),  
 141 which is applicable only for single-pol data, also to include  
 142 dual-pol data and optimize it to increase the density of SDFP  
 143 pixels for the time-series analysis. We then apply temporal  
 144 coherence in (2) to identify the SDFP pixels.

145 Fig. 2 shows a flowchart of the overall processing strategy  
 146 that is implemented in this letter. The method consists of three  
 147 main steps: 1) InSAR processing; 2) polarimetric optimization;  
 148 and (3) multitemporal analysis of the optimized interfero-  
 149 grams. Single-pol multitemporal InSAR analysis includes only  
 150 InSAR processing (step 1) and time-series analysis of the  
 151 interferograms (step 3). Polarimetric optimization is used here  
 152 to improve the performance of this analysis using dual-pol  
 153 data. In Section III we describe in detail the methodology we  
 154 used in our study.

## 155 III. ADD OPTIMIZATION

156 In order to obtain the polarimetric form of ADD it is  
 157 sufficient to replace the amplitude of single-pol data in (1)  
 158 by the polarimetric scattering coefficient,  $\mu$  defined as

$$159 \mu = \omega^{*T} \underline{K} \quad (3)$$

$$160 \underline{K} = \frac{1}{\sqrt{2}} [S_{hh} + S_{vv}, S_{hh} - S_{vv}]^T \quad (4)$$

$$161 \underline{\omega} = [\cos(\alpha) \quad \sin(\alpha) e^{j\psi}]^T, \quad 0 \leq \alpha \leq \pi/2, \quad -\pi \leq \psi \leq \pi \quad (5) \quad 162$$

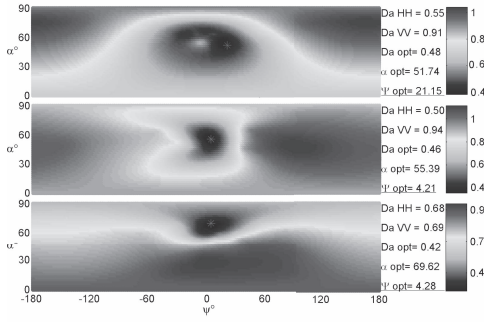


Fig. 3. Values of ADD for all possible values for  $\alpha$  and  $\psi$ , for three arbitrarily selected pixels. The red star presents the minimum value of ADD.

where  $K$  stands for the polarimetric vector,  $\omega$  is the polarimetric projection vector,  $S_{VV}$  and  $S_{HH}$  are the complex values of the HH and VV channels, respectively,  $T$  is the transpose operator and  $*$  denotes the conjugate operator.  $\alpha$  and  $\psi$  are Pauli parameters which represent the scattering mechanism [17], [22], [27]. The polarimetric form of ADD in (1) can then be written in the following form:

$$D_{\Delta A}^{\text{Pol}} = \frac{\sqrt{\sum_{i=1}^N (\Delta A_i^{\text{Pol}} - \overline{\Delta A^{\text{Pol}}})^2 / N}}{\sum_{i=1}^N (|\omega^{*T} K_i^M| + |\omega^{*T} K_i^S|) / 2N}$$

$$\Delta A^{\text{Pol}} = |\omega^{*T} K^M| - |\omega^{*T} K^S| \quad (6)$$

where  $K_i^M$  and  $K_i^S$  are polarimetric vectors of master and slave images, respectively.

The main objective of polarimetric optimization is to find the optimum scattering mechanism of the pixels and generate interferograms with better quality than using single-pol SAR images. To simplify the search of the optimum scattering mechanism, we parameterized the projection vector in terms of Pauli basis parameters. In order to build consistent time series of phases related to deformation we assume that the scattering mechanisms of the pixels remain the same during acquisition time, as in the case of multibaseline equal scattering mechanism. Therefore,  $\omega$  would be the same for the pixel in whole stack of interferograms [28].

The optimization problem is to find the projection vector that minimizes the value of ADD. Fig. 3 illustrates the possible ADD values, in terms of  $\alpha$  and  $\psi$ , for three arbitrarily selected pixels in our study area. In [17] we showed that SA is an effective method to minimize such smooth functions as illustrated in Fig. 3 and to find the optimum  $\alpha$  and  $\psi$  in their corresponding finite range. We define a coarse grid with a step size of  $10^\circ$  for both  $\alpha$  and  $\psi$  and search for the values that give the minimum ADD. These values for  $\alpha$  and  $\psi$  are then used as initial values in the SA optimization method.

#### IV. EXPERIMENTAL RESULTS AND DISCUSSION

To evaluate the method we processed 17 co-polar SAR images acquired by the TerraSAR-X satellite in an ascending mode between July 2013 and January 2014 over the Tehran plain, which is highly affected by subsidence [29]. We formed a small baseline network consisting of 44 single-look interferograms as shown in Fig. 4. We then generated interferograms for HH, VV and optimum channels and calculated the ADD value of each pixel in the single-look interferograms. To evaluate the improvement in ADD, we compared

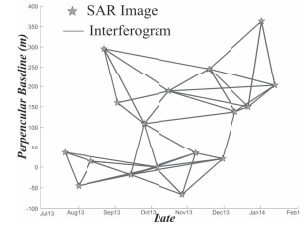


Fig. 4. Small baselines network used in this letter. The stars denote the SAR images and lines present the formed interferograms for Small Baseline processing.

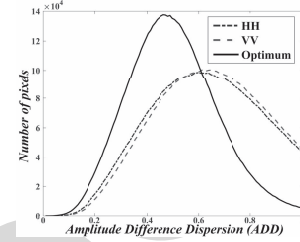


Fig. 5. Histograms of ADD for HH, VV and optimum channel.

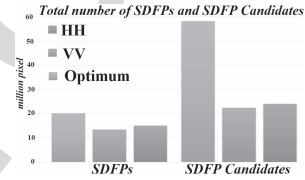


Fig. 6. Number of SDFP Candidates and SDFP pixels, obtained by HH, VV and optimum channel.

the histograms of ADD values for HH, VV and optimum channel (Fig. 5).

As shown in Fig. 5, by applying the proposed method, the histogram of ADD values in optimum channel is inclined to lower values of ADD in comparison to HH and VV channels. Therefore, by thresholding ADD value of less than 0.6, more SDFP candidates are extracted in optimum channel as compared to single-pole interferograms.

Fig. 6 depicts the number of selected SDFP candidates obtained from HH, VV and optimum channels using ADD criterion and also the improvement in number of SDFP pixels after utilizing temporal coherency.

The total number of SDFP candidates for the optimum channel is about 2.5 times higher than for the HH and VV channels. Considering the final selection of SDFP pixels for the optimum channel, the number has increased by about 1.4 times and 1.6 times in comparison to the HH and VV channels, respectively.

In order to evaluate the efficiency of using multitemporal polarimetric SAR data for different models of scattering we made a comparison between urban and nonurban regions. 46% of our study area comprises urban region, while the nonurban portion is about 54%. In urban areas, the number of identified candidates using the optimum channel is increased by  $\sim 1.7$  and  $\sim 2.1$  times compared to HH and VV channels, respectively. In regard to the agricultural regions, the increase is  $\sim 2.1$  and  $\sim 2.2$  times [Fig. 7(b)]. The number of final SDFP pixels increased  $\sim 1.4$  and  $\sim 1.5$  times in urban regions and  $\sim 1.48$  and  $\sim 1.65$  times in agricultural regions, in comparison

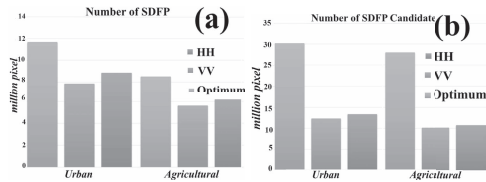


Fig. 7. Number of (a) identified SDFP pixels and (b) SDFP candidates detected in urban and agricultural regions using HH, VV and optimum.

TABLE I

QUANTITATIVE COMPARISON OF IDENTIFIED SDFP PIXELS WITH RESPECT TO PS PIXELS (EXPRESSED IN PERCENT OF PS PIXELS)

Dataset	Agricultural	Urban
HH	8.5 %	-9.0 %
VV	8.2 %	-8.9 %
Optimum	10.3 %	-7.9 %

to HH and VV channels, respectively [Fig. 7(a)]. Therefore the proposed algorithm is slightly more successful in nonurban regions than in urban regions.

As PS pixels and SDFP pixels relate to different scattering characteristics of the ground, we also compared the density of measurements for both of the methods in urban and nonurban regions. Table I describes the percentage of additional pixels identified by SDFP pixels in comparison with PS pixels for which the results were previously published in [17]. For the HH and VV channels we detect about 8% more SDFP pixels than PS in agricultural regions, however, over the urban area the number of identified SDFPs is almost 9% less than PS pixels.

Similar to the HH and VV channels, in the case of the optimum channel, the small baseline method detects 10% more coherent pixels in agricultural regions, while in urban area the PS pixels are more numerous than SDFP pixels by about 8%. SDFP pixels show little loss of correlation in short time intervals whereas PS pixels remain stable over the whole period of data acquisition. Therefore, in nonurban area more SDFP pixels are expected to be identified than PS pixels. By contrast, in urban areas PS pixels are more abundant. This might be related to the effect of filtering in the small baseline method, which increases the decorrelation in pixels dominated by a single scatterer as a result of coarsening the resolution of spectra [13].

In order to check that using the optimum channel leads to lower phase noise, we selected SDFP pixels approximately every  $0.001^\circ$  in both directions, and calculated the variance of the phase differences between the selected pixels and their immediate SDFP neighbors for the optimum, HH and VV channels. The results are shown in Fig. 8.

The standard deviation of differences are very similar for HH and VV, but are generally lower for the optimum channel, indicating that our method leads to reduced phase noise. There appear to be two populations of pixels, however; those for which the improvement is marginal and those for which the improvement is more significant [indicated in Fig 8(a)]. This division is not apparently related to scattering mechanism, but does appear to correlate with spatial position (Fig. 9), with pixels in urban areas, plotted in red, more likely to fall in the population with greatest improvement.

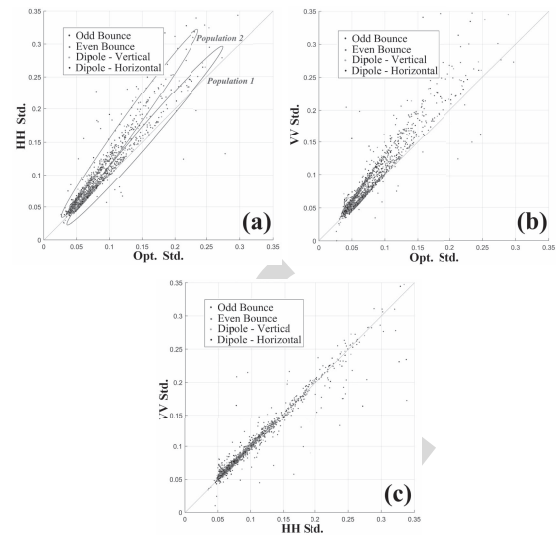


Fig. 8. Cross comparison of Standard deviation of phase differences of nearby SDFP pixels for the selected SDFP pixels for (a) HH versus Optimum channel, the two populations marked by green and red ellipse are spatially located in Fig. 9, (b) VV versus optimum channel, and (c) HH versus VV channel. Blue and red dots indicate odd-bounce and even-bounce scattering mechanisms, respectively. Green and black colors indicate vertical and horizontal dipole scattering mechanism, respectively.

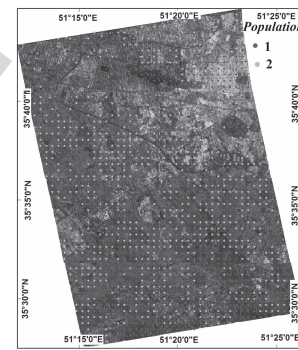


Fig. 9. Spatial position of the pixels in the two populations indicated in Fig. 8(a). Red circles depict the pixels located in the population where the reduction in standard deviation is most significant and the other population members are drawn in green.

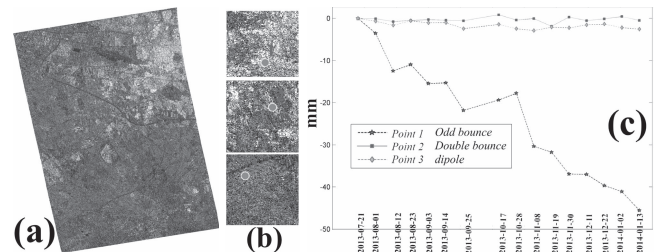


Fig. 10. (a) Location of the three points which detected by our method but not by using HH and VV. (b) Closer look of he points in (a), point 1 is located in a farming zone and shows odd-bounce mechanism, point 2 is located in an urban area with the dominant scattering mechanism for the pixel being double bounce and point 3 is a dipole. (c) Time series plot of the selected points.

Fig. 10 shows the time series for three sample SDFP pixels with odd-bounce (point 1), even-bounce (point 2) and dipole (point 3) scattering mechanisms, respectively,

that were selected using the optimal channel, but not when using HH and VV channels. The smoothness of each of the time series indicates that the phase values have a low contribution from noise and that our algorithm is not increasing the number of selected pixels simply by selecting more noisy pixels.

## V. CONCLUSION

StaMPS is a powerful method for multitemporal analysis of single-channel SAR images [13]. In this letter, we have presented a small baseline method, implemented in StaMPS, to deal with dual polarization SAR images. The ADD index criterion is first minimized for dual polarimetric data to find the optimum scattering mechanism that lead to increase the number of SDFP candidates. Then the results are combined with temporal coherence criteria to select final coherent pixels for time-series analysis. Our experiment in both urban and agricultural regions, shows that applying our method for dual-pol data increased the number of SDFP pixels by 50% in comparison to single-pol data InSAR time-series analysis. In addition, the assessment between the result of our proposed method for small baseline algorithm with those from PS-InSAR polarimetric optimization [17], showed that the density of SDFP pixels, in small baseline approach, is more than PS pixels in nonurban regions, while, in urban area the number of PS pixels is slightly higher than the SDFP pixels. Future research could focus on implementing this type of polarimetric optimization on full/quad polarimetry SAR images. Also, joint optimization using the PSI approach [17], [22] and our new algorithm could improve the ability to find stable points for a large range of ground scattering characteristics.

## ACKNOWLEDGMENT

Copyright of TerraSAR-X data belongs to German Aerospace Agency (DLR) and the data were provided by the project Motagh\_XTI\_LAND505.

## REFERENCES

- [1] F. Amelung, D. L. Galloway, J. W. Bell, H. A. Zebker, and R. J. Lacznik, "Sensing the ups and downs of Las Vegas: InSAR reveals structural control of land subsidence and aquifer-system deformation," *Geology*, vol. 27, no. 6, pp. 483–486, 1999.
- [2] G. Fornaro, A. Pauciuolo, and F. Serafino, "Deformation monitoring over large areas with multipass differential SAR interferometry: A new approach based on the use of spatial differences," *Int. J. Remote Sens.*, vol. 30, no. 6, pp. 1455–1478, 2009.
- [3] D. Massonnet *et al.*, "The displacement field of the Landers earthquake mapped by radar interferometry," *Nature*, vol. 364, no. 6433, pp. 138–142, Jul. 1993.
- [4] M. Motagh *et al.*, "Subduction earthquake deformation associated with 14 November 2007, Mw 7.8 Tocopilla earthquake in Chile: Results from InSAR and aftershocks," *Tectonophysics*, vol. 490, nos. 1–2, pp. 60–68, 2010.
- [5] H. A. Zebker and J. Villasenor, "Decorrelation in interferometric radar echoes," *IEEE Trans. Geosci. Remote Sens.*, vol. 30, no. 5, pp. 950–959, Sep. 1992.
- [6] A. Ferretti, C. Prati, and F. Rocca, "Nonlinear subsidence rate estimation using permanent scatterers in differential SAR interferometry," *IEEE Trans. Geosci. Remote Sens.*, vol. 38, no. 5, pp. 2202–2212, May 2000.
- [7] A. Ferretti, C. Prati, and F. Rocca, "Permanent scatterers in SAR interferometry," *IEEE Trans. Geosci. Remote Sens.*, vol. 39, no. 1, pp. 8–20, Jan. 2001.
- [8] A. Hooper, H. Zebker, P. Segall, and B. Kampes, "A new method for measuring deformation on volcanoes and other natural terrains using InSAR persistent scatterers," *Geophys. Res. Lett.*, vol. 31, no. 23, 2004.
- [9] P. Berardino, G. Fornaro, R. Lanari, and E. Sansosti, "A new algorithm for surface deformation monitoring based on small baseline differential SAR interferograms," *IEEE Trans. Geosci. Remote Sens.*, vol. 40, no. 11, pp. 2375–2383, Nov. 2002.
- [10] O. Mora, J. J. Mallorqui, and A. Broquetas, "Linear and nonlinear terrain deformation maps from a reduced set of interferometric SAR images," *IEEE Trans. Geosci. Remote Sens.*, vol. 41, no. 10, pp. 2243–2253, Oct. 2003.
- [11] D. A. Schmidt and R. Bürgmann, "Time-dependent land uplift and subsidence in the Santa Clara valley, California, from a large interferometric synthetic aperture radar data set," *J. Geophys. Res. Solid Earth*, vol. 108, no. B9, Sep. 2003.
- [12] R. Lanari, O. Mora, M. Manunta, J. J. Mallorqui, P. Berardino, and E. Sansosti, "A small-baseline approach for investigating deformations on full-resolution differential SAR interferograms," *IEEE Trans. Geosci. Remote Sens.*, vol. 42, no. 7, pp. 1377–1386, Jul. 2004.
- [13] A. Hooper, "A multi-temporal InSAR method incorporating both persistent scatterer and small baseline approaches," *Geophys. Res. Lett.*, vol. 35, no. 16, Aug. 2008.
- [14] S. R. Cloude and K. P. Papathanassiou, "Polarimetric SAR interferometry," *IEEE Trans. Geosci. Remote Sens.*, vol. 36, no. 5, pp. 1551–1565, Sep. 1998.
- [15] E. Colin, C. Titin-Schnaider, and W. Tabbara, "An interferometric coherence optimization method in radar polarimetry for high-resolution imagery," *IEEE Trans. Geosci. Remote Sens.*, vol. 44, no. 1, pp. 167–175, Jan. 2006.
- [16] P. Dheenathayalan and R. Hanssen, "Target characterization and interpretation of deformation using persistent scatterer interferometry and polarimetry," in *Proc. 5th Int. Workshop Sci. Appl. SAR Polarimetry Polarimetric Interferometry (PolinSAR)*, 2011, pp. 1–8.
- [17] M. Esmaeili and M. Motagh, "Improved persistent scatterer analysis using amplitude dispersion index optimization of dual polarimetry data," *J. Photogramm. Remote Sens.*, vol. 117, pp. 108–114, Jul. 2016.
- [18] S. Alipour, K. F. Tiampo, S. Samsonov, and P. J. Gonzalez, "Multi-baseline PolInSAR using RADARSAT-2 quad-pol data: Improvements in interferometric phase analysis," *IEEE Geosci. Remote Sens. Lett.*, vol. 10, no. 6, pp. 1280–1284, Nov. 2013.
- [19] D. Monells, J. Mallorqui, G. Centolanza, and C. Lopez-Martinez, "Application of polarimetric techniques in DinSAR processing for space borne subsidence monitoring," in *Proc. Sci. Appl. SAR Polarimetry Polarimetric Interferometry (PolinSAR)*, vol. 695, 2011, pp. 1–22.
- [20] L. Pipia *et al.*, "Polarimetric differential SAR interferometry: First results with ground-based measurements," *IEEE Geosci. Remote Sens. Lett.*, vol. 6, no. 1, pp. 167–171, Jan. 2009.
- [21] V. D. Navarro-Sanchez and J. M. López-Sanchez, "Subsidence monitoring using polarimetric persistent scatterers interferometry," in *Proc. IEEE Int. Geosci. Remote Sens. Symp. (IGARSS)*, Jul. 2011, pp. 1083–1086.
- [22] V. D. Navarro-Sanchez and J. M. Lopez-Sanchez, "Improvement of persistent-scatterer interferometry performance by means of a polarimetric optimization," *IEEE Geosci. Remote Sens. Lett.*, vol. 9, no. 4, pp. 609–613, Jul. 2012.
- [23] V. D. Navarro-Sanchez, J. M. Lopez-Sanchez, and L. Ferro-Famil, "Polarimetric approaches for persistent scatterers interferometry," *IEEE Trans. Geosci. Remote Sens.*, vol. 52, no. 3, pp. 1667–1676, Mar. 2014.
- [24] S. Samsonov and K. Tiampo, "Polarization phase difference analysis for selection of persistent scatterers in SAR interferometry," *IEEE Geosci. Remote Sens. Lett.*, vol. 8, no. 2, pp. 331–335, Mar. 2011.
- [25] R. Iglesias, D. Monells, X. Fabregas, J. J. Mallorqui, A. Aguiasca, and C. López-Martinez, "Phase quality optimization in polarimetric differential SAR interferometry," *IEEE Trans. Geosci. Remote Sens.*, vol. 52, no. 5, pp. 2875–2888, May 2014.
- [26] B. Wu, T. Ling, Y. Chen, and H. Lei, "New methods in multibaseline polarimetric SAR interferometry coherence optimization," *IEEE Geosci. Remote Sens. Lett.*, vol. 12, no. 10, pp. 2016–2020, Oct. 2015.
- [27] S. R. Cloude and K. P. Papathanassiou, "Polarimetric optimisation in radar interferometry," *Electron. Lett.*, vol. 33, no. 13, pp. 1176–1178, Jun. 1997.
- [28] M. Neumann, L. Ferro-Famil, and A. Reigber, "Multibaseline polarimetric SAR interferometry coherence optimization," *IEEE Geosci. Remote Sens. Lett.*, vol. 5, no. 1, pp. 93–97, Jan. 2008.
- [29] M. Motagh *et al.*, "Land subsidence in Iran caused by widespread water reservoir overexploitation," *Geophys. Res. Lett.*, vol. 35, no. 16, Aug. 2008.

AQ:4



AQ:6

AQ:5

## AUTHOR QUERIES

### AUTHOR PLEASE ANSWER ALL QUERIES

**PLEASE NOTE:** We cannot accept new source files as corrections for your paper. If possible, please annotate the PDF proof we have sent you with your corrections and upload it via the Author Gateway. Alternatively, you may send us your corrections in list format. You may also upload revised graphics via the Author Gateway.

Please be aware that authors are required to pay overlength page charges (\$200 per page) if the paper is longer than 3 pages. If you cannot pay any or all of these charges please let us know.

This pdf contains 2 proofs. The first half is the version that will appear on Xplore. The second half is the version that will appear in print. If you have any figures to print in color, they will be in color in both proofs.

The “Open Access” option for your paper expires when the paper is published on Xplore in an issue with page numbers. Papers in “Early Access” may be changed to Open Access.

If you have not completed your electronic copyright form (ECF) and payment option please return to Scholar One “Transfer Center.” In the Transfer Center you will click on “Manuscripts with Decisions” link. You will see your article details and under the “Actions” column click “Transfer Copyright.” From the ECF it will direct you to the payment portal to select your payment options and then return to ECF for copyright submission.

AQ:1 = Please provide the expansion for “InSAR.”

AQ:2 = Please provide the postal code for “University of Tehran, Tehran, Iran.”

AQ:3 = Please provide the country name for “the GFZ German Research Center for Geosciences.”

AQ:4 = Please confirm whether the retention of this sentence in the acknowledgment section is ok.

AQ:5 = Please provide the page range for refs. [8], [11], [13], and [29].

AQ:6 = Please confirm the author names, article title, conference title, volume no., page range, and year for ref. [19].